A hybrid immersed boundary and immersed interface method for electrohydrodynamic simulations

Wei-Fan Hu [a], Ming-Chih Lai [b,*], Yuan-Nan Young [c]

[a] *Department of Applied Mathematics, National Chiao Tung University, 1001, Ta Hsueh Road, Hsinchu 300, Taiwan*
[b] *Center of Mathematical Modeling and Scientific Computing & Department of Applied Mathematics, National Chiao Tung University, 1001, Ta Hsueh Road, Hsinchu 300, Taiwan*
[c] *Department of Mathematical Sciences, New Jersey Institute of Technology, Newark, NJ 07102, USA*

A B S T R A C T

In this paper, we develop a hybrid immersed boundary (IB) and immersed interface method (IIM) to simulate the dynamics of a drop under an electric field in Navier–Stokes flows. Within the leaky dielectric framework with piecewise constant electric properties in each fluid, the electric stress can be treated as an interfacial force on the drop interface. Thus, both the electric and capillary forces can be formulated in a unified immersed boundary framework. The electric potential satisfies a Laplace equation which is solved numerically by an augmented immersed interface method which incorporates the jump conditions naturally along the normal direction. The incompressible Navier–Stokes equations for the fluids are solved using a projection method on a staggered MAC grid and the potential is solved at the cell center. The interface is tracked in a Lagrangian manner with mesh control by adding an artificial tangential velocity to transport the Lagrangian markers to ensure that the spacing between markers is uniform throughout the computations. A series of numerical tests for the present scheme have been conducted to illustrate the accuracy and applicability of the method. We first compute the potential and its gradient (electric field) to perform the accuracy check for the present augmented IIM. We then check the convergence of the interfacial electric force and the fluid variables. We further run a series of simulations with different permittivity and conductivity ratios and compare with the results obtained by the small deformation theory and other numerical results in literature. In addition, we also study the electric effect for a drop under shear flow.

© 2014 Elsevier Inc. All rights reserved.

1. Introduction

The study of hydrodynamics driven by an electric field (electrohydrodynamics) has many industrial applications in micro-fluidic systems [22,33]. In particular, a weakly conducting (leaky dielectric) drop suspended in another leaky dielectric fluid under an electric field (as depicted in Fig. 1) has been extensively studied from different perspectives. G.I. Taylor [27] concluded that the equilibrium drop shape can be explained by balancing the viscous stress with the electric stress on the drop interface as long as he took into account the induced surface charges due to the mismatch in electric conductivity and permittivity between the two fluids. Furthermore, it is found that drop can be deformed into either a prolate or an oblate

---

equilibrium shape with circulatory flows inside the drop [20]. The drop deformation and flow patterns mainly depend on the electrical properties of the fluid system. A comprehensive review of further theoretical developments can be found in [24]. Most theoretical models are limited to small deformation from a spherical drop under moderate electric fields, and such limitation leads to quantitative discrepancies reported in [29]. Recently a spheroidal model was used to study the large electrodeformation of a leaky dielectric drop (see [21] and references therein). Results from these models agree well with experiments up to moderate electric capillary number. However, these spheroidal models still cannot predict the drop deformation under large electric field strengths.

Thus, there has been a continuing interest in using numerical methods to simulate the electrohydrodynamics of a viscous drop under an electric field. Numerous works on the numerical simulations of drop deformations under leaky dielectric theory are reported in the literature. Based on how the interface is treated, these works can be categorized into the front tracking method [11,30], level set method [4,31], phase field method [18,35], and the volume-of-fluid method [9,32]. Other numerical approaches include lattice Boltzmann method [36] and boundary integral method [13,25], just to name a few.

In this paper, a hybrid immersed boundary (IB) and immersed interface method (IIM) are developed to simulate the dynamics of a leaky dielectric drop under an electric field in Navier–Stokes fluids. The immersed boundary method used to solve the fluid equations is similar in spirit to the front-tracking method as in [11,30]. Other recent immersed boundary methods to study particle–particle interactions in electrohydrodynamics can be found in [3,10], in particular, the former one used the available immersed interface method solver [17] to solve the potential equation but the applications and the electric force calculations are different from the present study.

The major contributions and significant differences of our work from previous works [4,3,11,10,18,30–32,35] are as follows. Firstly, the Maxwell stress tensor arising from the electric effect is cast as an interfacial electric force (the jump of Maxwell tensor across the interface) rather than the volume force in the equations so that the capillary and electric interfacial forces can be formulated in a unified immersed boundary framework. As can be seen in the next section (Section 2), the present approach avoids applying the divergence operator to the Maxwell tensor. This is particularly important since the tensor is discontinuous across the interface due to different permittivity and conductivity.

Secondly, a sharp immersed interface method is used to compute the potential and its gradient. One-sided interpolations to the interface from either side are used to obtain the Maxwell stress tensor (thus the interfacial electric force) more accurately. In most aforementioned works in literature, the electric potential equation Eq. (6) is solved numerically by smoothing the piecewise conductivity σ over a narrow region using the harmonic means without any special treatments near the interface. However, according to the jump condition Eq. (7), one can immediately see that $\nabla\phi$ has nonzero jump across the interface. Thus, by the above smoothing numerical method, the electric field $\mathbf{E} = -\nabla\phi$ will have $O(1)$ error near the interface. Furthermore, the smoothing of permittivity ε also causes $O(1)$ error near the interface. The computations of $\nabla\varepsilon$ and $\nabla \cdot (\varepsilon\mathbf{E})$ both have $O(1/h)$ error near the interface. As a result, the direct calculation of volume electric force Eq. (9) is not accurate near the interface. Here, instead of computing the volume force, we compute the interfacial electric force in a more accurate manner. We are also able to demonstrate the numerical convergence of this interfacial force. A more rigorous theoretical analysis on the accuracy of finite difference schemes for elliptic interface problems can be found in [2].

The paper is organized as follows. The governing equations for the electrohydrodynamics within the leaky dielectric framework are presented in Section 2. A simple version of augmented immersed interface method for solving piecewise elliptic interface problem is introduced and tested in Section 3. A hybrid numerical algorithm of immersed boundary and immersed interface methods for solving the electrohydrodynamics equations is outlined in Section 4. The numerical results consisting of convergence check and drop deformations under DC electric fields with different permittivities and conductivities are studied in detail in Section 5. Some concluding remarks and brief discussion on future directions are given in Section 6.

2. Governing equations of electrohydrodynamics

In this paper, we consider a leaky dielectric drop (Ω^-) suspended in another immiscible leaky dielectric fluid (Ω^+) under a DC (direct current) electric field $\mathbf{E}_\infty$ as depicted in Fig. 1. The governing equations consist of two-dimensional incompressible Navier–Stokes equations with surface tension and electric forces. We further assume that both the density and viscosity are identical for the drop and suspended fluid as we concentrate more on the electro-deformation of the drop due to different electric conductivity and permittivity. The drop is neutrally buoyant in the fluid domain Ω and the gravitational force is neglected. The fluid interface Σ is represented by a Lagrangian parametric form $\mathbf{X}(s,t) = (X(s,t), Y(s,t))$, $0 \le s \le 2\pi$, where s is the parameter of the initial configuration of the interface. Under the immersed boundary formulation, this two-fluid system is cast as a single fluid with variable physical properties in a single domain $\Omega = \Omega^- \cup \Omega^+$

$$\rho(\frac{\partial \mathbf{u}}{\partial t} + (\mathbf{u} \cdot \nabla)\mathbf{u}) + \nabla p = \mu \Delta \mathbf{u} + \mathbf{f}_C + \mathbf{f}_E \quad \text{in } \Omega, \tag{1}$$

$$\nabla \cdot \mathbf{u} = 0 \quad \text{in } \Omega, \tag{2}$$

$$\frac{\partial \mathbf{X}}{\partial t}(s,t) = \mathbf{U}(s,t) = \int_\Omega \mathbf{u}(\mathbf{x},t)\delta(\mathbf{x} - \mathbf{X}(s,t)) \, d\mathbf{x} \quad \text{on } \Sigma. \tag{3}$$
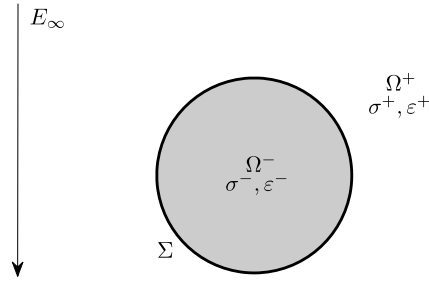
Fig. 1. A leaky dielectric drop suspended in another leaky dielectric fluid under DC electric field.

Eqs. (1)–(2) are the familiar incompressible Navier–Stokes equations with the fluid density ρ, the velocity $\mathbf{u}$, the pressure p, the dynamic viscosity μ, the capillary force arising from the interfacial tension $\mathbf{f}_C$, and the electric force $\mathbf{f}_E$. Eq. (3) simply states that the interface moves along with the local fluid velocity (the interfacial velocity) which is linked by the two-dimensional Dirac delta function $\delta(\mathbf{x}) = \delta(x)\delta(y)$.

The capillary force due to tension on the interface is immersed as

$$\mathbf{f}_C(\mathbf{x}, t) = \int_{\Sigma} \frac{\partial}{\partial s}(\gamma \boldsymbol{\tau}) \, \delta\big(\mathbf{x} - \mathbf{X}(s, t)\big) \, \mathrm{d}s, \tag{4}$$

where γ is the surface tension, and $\boldsymbol{\tau} = \frac{\mathbf{X}_s}{|\mathbf{X}_s|}$ is the unit tangent vector along the interface. Here, the subscript in $\mathbf{X}_s$ denotes the partial derivative of $\mathbf{X}$ with respect to s. In case of a surfactant-covered drop considered, the surface tension γ may not be a constant and it depends on the surfactant concentration via Langmuir equation of state. For such case, an extra surfactant convection–diffusion equation must be incorporated into the fluid system. One of the authors (M.-C. Lai) and his group have developed a numerically conservative scheme for solving the insoluble [15] and soluble surfactant equations [5]. The electric force $\mathbf{f}_E$ for the leaky dielectric model will be given in the next section.

2.1. Leaky dielectric model

In electrohydrodynamics, the dynamic current (with dimension I) is usually small so the induced magnetic effect can be neglected. Thus, the electric field intensity $\mathbf{E}(MLT^{-3}I^{-1})$ is irrotational which results in $\nabla \times \mathbf{E} = 0$. By Gauss law in a dielectric material with permittivity $\varepsilon(M^{-1}L^{-3}T^4I^2)$, the volume charge density $q_v(L^{-3}TI)$ can be written as $q_v = \nabla \cdot (\varepsilon \mathbf{E})$. The conservation of free charge density in electrohydrodynamics can be expressed as

$$\frac{Dq_v}{Dt} + \nabla \cdot (\sigma \mathbf{E}) = 0, \tag{5}$$

where $\frac{D}{Dt} = \frac{\partial}{\partial t} + \mathbf{u} \cdot \nabla$ is the material derivative and $\sigma(M^{-1}L^{-3}T^3I^2)$ is the electric conductivity of the medium. In a homogeneous incompressible fluid where the permittivity ε and conductivity σ are both constant, one can show that the free charge density decays from the initial charge density with the relaxation time scale $t_E = \varepsilon/\sigma$ [20]. The viscous time scale of the fluid motion is defined by $t_F = \rho L^2/\mu$, where ρ and μ are fluid density and viscosity, and L is the characteristic length scale.

In a leaky dielectric model [20,24] for a two-fluid system with different electric properties depicted in Fig. 1, the charge accumulates at the fluid interface almost instantaneously as compared to the time scale of the fluid motion ($t_E \ll t_F$). Thus, the bulk charge density equation (5) can be simplified into

$$\nabla \cdot (\sigma \mathbf{E}) = 0, \quad \text{in } \Omega \setminus \Sigma. \tag{6}$$

With piecewise constant of the electric conductivity σ^- (in Ω^-) and σ^+ (in Ω^+) respectively, one concludes that $\nabla \cdot \mathbf{E} = 0$ in both domains Ω^- and Ω^+. Since the electric field $\mathbf{E}$ is irrotational ($\nabla \times \mathbf{E} = 0$) as mentioned earlier, the electric field can be expressed in terms of electric potential ϕ by $\mathbf{E} = -\nabla \phi$. Therefore, Eq. (6) can be further reduced to Laplace equation for the potential ϕ in each fluid domain Ω^- and Ω^+. In the far field, a constant electric field $\mathbf{E}_\infty$ is applied to the fluid system.

The boundary conditions along the interface Σ separating Ω^- and Ω^+ are based on the continuity of the electric potential and the normal component of the electric flux density across the interface:

$$[\phi] = 0 \quad \text{and} \quad [\sigma \nabla \phi \cdot \mathbf{n}] = 0 \quad \text{on } \Sigma, \tag{7}$$

where the jump $[\cdot]$ indicates the quantity from the Ω^+ side minus the one of Ω^- side, and the normal vector $\mathbf{n}$ is pointing outward from Ω^- to Ω^+ side. The permittivity of drop and the suspended fluid are piecewise constant and denoted by ε^- and ε^+, respectively. A sketch of the problem setup is depicted in Fig. 1.

As described in [20,24], the stress induced in a dielectric medium under an electric field is given by the Maxwell stress tensor of the form

$$\mathbf{M}_E = \varepsilon \left(\mathbf{EE} - \frac{1}{2} (\mathbf{E} \cdot \mathbf{E}) I \right). \tag{8}$$

The equivalent volume force density of the Maxwell stress can be obtained by taking the divergence of above equation so we have

$$\mathbf{f}_E = \nabla \cdot \mathbf{M}_E = -\frac{1}{2} (\mathbf{E} \cdot \mathbf{E}) \nabla \varepsilon + \nabla \cdot (\varepsilon \mathbf{E}) \mathbf{E}. \tag{9}$$

The first term on the right-hand side of the above equation is due to polarization stress and it acts along the normal direction of the interface. The second term is due to the interaction of the electric charges under the direction of the electric field. Since both the permittivity and conductivity are piecewise constant, one immediately sees that the electric force in Eq. (9) is non-zero only in the vicinity of the interface due to the fact of $\nabla \cdot \mathbf{E} = 0$ in both domains Ω^- and Ω^+. Therefore for our modeling purpose, we regard the electric effect as an interfacial force from the jump of Maxwell stress in the normal direction instead of applying the volume force as in Eq. (9) into the fluid equations. The interfacial electric force is defined as

$$\mathbf{F}_E = [\mathbf{M}_E \cdot \mathbf{n}] = \left(\mathbf{M}_E^+ - \mathbf{M}_E^- \right) \cdot \mathbf{n}, \tag{10}$$

where $\mathbf{M}_E^-$ and $\mathbf{M}_E^+$ stand for Maxwell stress tensor in the drop and the suspended fluid, respectively. Thus, the electric volume force $\mathbf{f}_E$ can be alternatively represented by the electric interfacial force using the Dirac delta function as

$$\mathbf{f}_E(\mathbf{x}, t) = \int\limits_{\Sigma} \mathbf{F}_E(s, t) \delta \left(\mathbf{x} - \mathbf{X}(s, t) \right) |\mathbf{X}_s| \, ds. \tag{11}$$

It is quite interesting to conclude that the interfacial electric force in Eq. (10) has exactly the same form as the continuous electric surface force derived by Tomar et al. [32] in which the authors take the limit of vanishing transition region thickness to be zero. The explicit form of the present interfacial electric force in Eq. (10) will be derived in detail in Appendix A. Note also that, this kind of interfacial force approach is especially necessary to numerical simulations for boundary integral method such as in [13] and has been adopted by McConnell and Miksis in [19] for vesicle electrohydrodynamic simulations.

3. A simple version of immersed interface method for solving elliptic interface problem

In this section, we propose a simple version of immersed interface method for solving the electric potential equation Eq. (6) in a domain Ω with jump conditions across the interface Σ (Eq. (7)). We consider the problem on a rectangular computational domain $\Omega = [a, b] \times [c, d]$ with an immersed interface $\Sigma = \{\mathbf{X}(s) = (X(s), Y(s)), 0 \le s < 2\pi\}$, where s is a Lagrangian parameter and $\mathbf{X}(0) = \mathbf{X}(2\pi)$. The interface Σ divides the domain Ω into two regions; namely inside (Ω^-) and outside (Ω^+) of the interface. Without loss of generality, we consider the following elliptic interface problem with inhomogeneous jumps as

$$\nabla \cdot (\sigma \nabla \phi) = f \quad \text{in } \Omega \setminus \Sigma, \quad [\phi] = v, \quad [\sigma \nabla \phi \cdot \mathbf{n}] = w, \quad \text{on } \Sigma. \tag{12}$$

Of course, the above equation should be accompanied with some suitable boundary condition (say Dirichlet or Neumann condition) along the computational domain $\partial \Omega$. Other boundary conditions will not change the main ingredients presented here. Note that, the jumps $v(s)$ and $w(s)$ are both functions defined on the interface Σ. Since σ is piecewise constant, we can rewrite the above equation in the form of Poisson equation $\Delta \phi = f / \sigma$ in different domains Ω^+ and Ω^- with the same jump conditions. In the following, we use the shorthand ϕ_n to represent the normal derivative $\nabla \phi \cdot \mathbf{n}$. In order to apply the scheme developed in [23,14] directly, the jump conditions $[\phi]$ and $[\phi_n]$ must be known and given. However, the jump in normal derivative $[\phi_n]$ is unknown. We thus introduce an augmented unknown variable $[\phi_n] = g$ into the system as in [17] such that the solution satisfies the piecewise jump condition $[\sigma \phi_n] = w$. In summary, Eq. (12) becomes the following elliptic interface problem as

$$\Delta \phi = \begin{cases} f^- / \sigma^- & \text{in } \Omega^- \\ f^+ / \sigma^+ & \text{in } \Omega^+ \end{cases} \quad [\phi] = v, \quad [\phi_n] = g, \quad [\sigma \phi_n] = w, \quad \text{on } \Sigma. \tag{13}$$

After some simple calculations, the relation between the jumps of $[\phi_n]$ and $[\sigma \phi_n]$ can be expressed by either one of

$$\phi_n^+ + \frac{\sigma^-}{[\sigma]} [\phi_n] = \frac{[\sigma \phi_n]}{[\sigma]}, \quad \text{if } \sigma^- > \sigma^+, \quad \text{or} \tag{14}$$

$$\phi_n^- + \frac{\sigma^+}{[\sigma]} [\phi_n] = \frac{[\sigma \phi_n]}{[\sigma]}, \quad \text{if } \sigma^+ > \sigma^-. \tag{15}$$

The above choice is proposed by Xu [34] which will become clear in our numerical scheme discussed later.
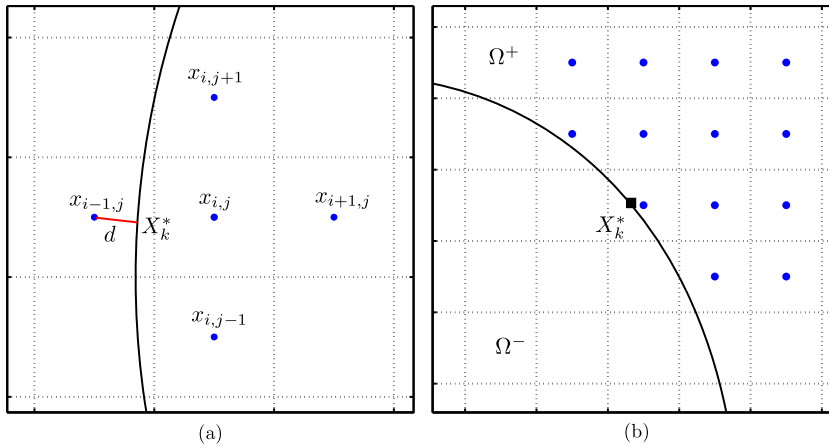
Fig. 2. (a) The grid points used in five-point Laplacian at the irregular point $\mathbf{x}_{ij}$ might cross the interface. (b) A grid layout indicating the neighboring grid points used in least squares cubic polynomial approximation to the one-sided normal derivative at $\mathbf{X}_k^*$.

3.1. An augmented IIM to incorporate the jumps in the normal direction

In this subsection, we introduce an augmented approach for elliptic interface problems described in previous subsection. Our technique is similar to the one in [17] but the computational details of the correction terms are quite different. To proceed, let us first lay out a uniform Cartesian grid in Ω with mesh width $h = \Delta x = \Delta y$. The grid points $\mathbf{x}_{ij}$ are defined at the cell center where the discrete solutions ϕ_{ij} are located. As in [17], we classify the grid point as either a regular or irregular point. For a regular grid point, we mean that the standard five-point Laplacian at that point does not cut through the interface. On the other hand, if the five-point Laplacian of a grid point involves using the grid points inside and outside the interface simultaneously, then we call it an irregular point. Since the solution is smooth either inside or outside the drop, the five-point Laplacian of a regular point does not need to be modified in order to have the second-order accuracy. However, a modification is needed at an irregular point where the solution is not smooth across the interface. The modification depends on the jump conditions $[\phi]$ and $[\phi_n]$. Thus, the discretization of Eq. (13) at the grid point $\mathbf{x}_{ij}$ can be generally written in the form of

$$\Delta_h \phi_{ij} + \frac{C_{ij}}{h^2} = \overline{f}_{ij}, \tag{16}$$

where C_{ij} is the correction term which is nonzero only if the grid point is irregular.

Let us briefly describe how the correction term is derived at this particular irregular point as illustrated in Fig. 2(a). When we apply the five-point Laplacian to $\mathbf{x}_{ij}$, the grid point $\mathbf{x}_{i-1,j}$ falls into the different side of the interface so the main source of correction comes only from the point $\mathbf{x}_{i-1,j}$. To derive the correction term as in [14,23], we first need to find the orthogonal projection of $\mathbf{x}_{i-1,j}$ on the interface (say $\mathbf{X}_k^* = \mathbf{X}(s_k^*)$ as shown in Fig. 2(a)), and then apply the truncated Taylor's series expansion along the normal direction at $\mathbf{X}_k^*$. The correction term thus becomes

$$C_{ij} = [\phi]_{\mathbf{X}_k^*} + d\,[\phi_n]_{\mathbf{X}_k^*} + \frac{d^2}{2}\left([\overline{f}] - \kappa\,[\phi_n] - \frac{1}{|\mathbf{X}_s|}\frac{\partial}{\partial s}\left(\frac{1}{|\mathbf{X}_s|}\frac{\partial[\phi]}{\partial s}\right)\right)_{\mathbf{X}_k^*}, \tag{17}$$

where the value d is the signed distance between the grid point $\mathbf{x}_{i-1,j}$ and its orthogonal projection $\mathbf{X}_k^*$, and κ is the local curvature of the interface. Note that, for a fixed interface, the curvature is known at those orthogonal projection points. However, when the interface is evolving as present applications, the curvature at those projection points can be computed by the cubic spline interpolation of the ones at the neighboring Lagrangian markers. We leave the details on how to compute the local curvature at Lagrangian markers in Section 4. Let Φ and Ψ be the solution vectors formed by ϕ_{ij} and $[\phi_n]_{\mathbf{X}_k^*}$, then the difference equation has the matrix form $A\Phi + E\Psi = F$.

Note that, in the calculation of the correction term C_{ij}, all the terms are basically available except the normal derivative jump $[\phi_n]_{\mathbf{X}_k^*}$ which can be linked to the known jump $[\sigma\phi_n]_{\mathbf{X}_k^*}$ through Eqs. (14) or (15). However, an approximation to $\phi_n^+(\mathbf{X}_k^*)$ or $\phi_n^-(\mathbf{X}_k^*)$ is needed. Here, we use the least squares cubic polynomial approach to approximate those values as follows. First, we choose the neighboring grid points of $\mathbf{X}_k^* = (X_k^*, Y_k^*)$ such as the ones depicted in Fig. 2(b), and then use the values of ϕ_{ij} at those grid points to construct the least squares cubic polynomial $P(x, y)$. Thus, the value of $\phi_n^+(\mathbf{X}_k^*)$ can be approximated by computing $\nabla P(\mathbf{X}_k^*) \cdot \mathbf{n}(\mathbf{X}_k^*)$ directly. This least squares cubic polynomial approach has third-order of accuracy to the approximation of the function itself while the derivative has second-order of accuracy. Notice that, in our present numerical experiments, the above approach to approximate $\phi_n^+(\mathbf{X}_k^*)$ has better accuracy than the one-sided normal extrapolation formula proposed by Xu in [34].

The approximation for ϕ_n^- can be done in a similar manner so we omit it here. With this approximation, we can rewrite Eqs. (14)–(15) in a matrix form as $B^\pm \Phi + \frac{\sigma^\mp}{[\sigma]}\Psi = G$, where B^+ and B^- denote the matrices resulting from the above least squares cubic polynomial approximation along the outward and inward normal directions, respectively. Note that, we do not form the matrix $B^\pm$ explicitly in practice since the GMRES iteration is applied to solve the above linear system in the following solution procedures. The vector G is the known jumps at those orthogonal projections $\mathbf{X}_k^*$. Thus, the resultant linear system becomes

$$\begin{bmatrix} A & E \\ B^\pm & \frac{\sigma^\mp}{[\sigma]}I \end{bmatrix}\begin{bmatrix} \Phi \\ \Psi \end{bmatrix} = \begin{bmatrix} F \\ G \end{bmatrix}. \tag{18}$$

Although the above augmented technique is similar to the one developed in [34], the linear system in Eq. (18) is solved differently. In [34], the author first eliminated the unknown Ψ to obtain the equation for Φ; and then solved the resultant linear system by pseudo time iteration to steady state. Here, we first eliminate Φ from Eq. (18) to obtain a linear system of Ψ

$$\left(B^\pm A^{-1}E - \frac{\sigma^\mp}{[\sigma]}I\right)\Psi = B^\pm\left(A^{-1}F\right) - G. \tag{19}$$

This is an $N_b \times N_b$ system for Ψ where N_b is the number of the projection points used on the interface. The order of above linear system is one-dimension lower than the one for solving Φ. We then use the GMRES iterative method to solve the above linear system. Since the GMRES method only requires the matrix-vector multiplication, it is not necessary to construct the matrices A and $B^\pm$ explicitly. In each GMRES iteration, the inversion of A can be performed efficiently by applying the fast Poisson solver provided by Fishpack [1] public software package. The detailed numerical algorithm can be split into the following three steps.

Step 1. Apply one fast Poisson solver to solve Φ^* in

$$A\Phi^* = F.$$

Step 2. Apply GMRES iterative method to solve Ψ until it converges in

$$\left(B^\pm A^{-1}E - \frac{\sigma^\mp}{[\sigma]}I\right)\Psi = B^\pm\Phi^* - G.$$

Step 3. Apply one fast Poisson solver to solve Φ in

$$A\Phi = F - E\Psi.$$

As mentioned before, the usage of Eq. (14) or Eq. (15) depends on the ratio of $\sigma_r = \sigma^-/\sigma^+$. If $\sigma_r > 1$, then we use Eq. (14) to compute $[\phi_n]$; otherwise, we use Eq. (15). One can easily compute that $\sigma^-/[\sigma] = \sigma_r/(1 - \sigma_r)$ and $\sigma^+/[\sigma] = 1/(1 - \sigma_r)$. The reason of the above choice is to ensure that the coefficient of diagonal matrix $\frac{\sigma^\mp}{[\sigma]}I$ has larger magnitude so that the matrix tends to be more diagonally dominant. In such way, the GMRES iterative method can converge quickly. Here, we set the stopping criteria for GMRES method as h^2 since the correction term is now with local truncation error $O(h)$. Thus, the overall computational cost for Steps 1–3 in our present scheme can be evaluated in terms of the number of fast Poisson solvers being applied.

3.2. Numerical tests

Example 1 (*Convergence and efficiency test*). In this test, we demonstrate the accuracy and efficiency of the present augmented IIM by choosing a given analytical solution for Eq. (12) in $\Omega = [-1, 1] \times [-1, 1]$ as

$$\phi(x, y) = \begin{cases} \exp(x + y) & \mathbf{x} \in \Omega^-, \\ \sin x \sin y & \mathbf{x} \in \Omega^+. \end{cases}$$

The interface is chosen as an ellipse $(\frac{x}{0.2})^2 + (\frac{y}{0.5})^2 = 1$ so that the jump discontinuities v and w in Eq. (12) can be exactly computed as well. For simplicity, here the Dirichlet boundary conditions are used because an exact solution is available. In Table 1, we show the mesh refinement results for the solution and its derivatives with conductivity ratio $\sigma_r = 10$ and 0.1, respectively. The mesh width is defined as $h = 2/N$ in both x and y directions with the grid size N. Note that, the derivatives ϕ_x and ϕ_y are defined at the cell edges and computed by the standard centered difference scheme using the computed solutions of two adjacent grid points. At the irregular point, a correction term has to be added as in [14]. This can be done straightforwardly here since the jump $[\phi_n]$ is also solved in our numerical algorithm. As shown in Table 1, the rate of convergence for the solution ϕ is around second-order while the derivatives ϕ_x and ϕ_y are slightly less than second-order. As for the computational complexity, one can see from the last column of Table 1 that the number of GMRES iterations plateaus to 10 as the grid size doubles. All the numerical computations were carried out on a PC with Intel Core i7 CPU

Table 1

The accuracy and efficiency results for the numerical solution ϕ_h and its derivatives $(\phi_h)_x$ and $(\phi_h)_y$ as the mesh is refined. Here, ϕ_e is the exact solution so its derivatives $(\phi_e)_x$ and $(\phi_e)_y$ can be computed directly.

N	$\|\phi_h - \phi_e\|_\infty$	Rate	$\|(\phi_h)x - (\phi_e)x\|_\infty$	Rate	$\|(\phi_h)_y - (\phi_e)_y\|_\infty$	Rate	Iter.
$\sigma_r = 10$							
32	3.31E−04	–	2.51E−03	–	1.75E−03	–	7
64	8.46E−05	1.97	3.42E−04	2.88	3.84E−04	2.19	9
128	2.43E−05	1.80	9.85E−05	1.80	1.13E−04	1.76	10
256	5.37E−06	2.18	3.84E−05	1.36	3.50E−05	1.69	10
$\sigma_r = 0.1$							
32	7.99E−04	–	5.07E−03	–	5.16E−03	–	6
64	1.27E−04	2.65	5.21E−04	3.28	6.10E−04	3.08	6
128	3.08E−05	2.04	1.91E−04	1.45	2.52E−04	1.28	7
256	5.37E−06	2.52	2.85E−05	2.74	3.12E−05	3.01	7

Table 2

The mesh refinement results between the present IIM (denoted by ϕ_h) and the smoothing method (denoted by ϕ_h^S) with ratio $\sigma_r = 0.1$.

N	$\|\phi_h - \phi_e\|_\infty$	$\|\phi_h^S - \phi_e\|_\infty$	$\|(\phi_h)_x - (\phi_e)_x\|_\infty$	$\|(\phi_h^S)_x - (\phi_e)_x\|_\infty$
32	3.07E−03	2.84E−02	1.45E−03	6.34E−01
64	7.72E−04	8.57E−03	4.44E−04	5.91E−01
128	1.93E−04	4.28E−03	1.10E−04	6.32E−01
256	4.84E−05	2.45E−03	2.85E−05	6.80E−01

and 16G RAM. The computational cost for the present fast Poisson solver is $O(N^2 \log N)$ with the grid size N in both x and y directions. The total CPU running time for each numerical result listed in Table 1 is within a second even with the grid size $N = 256$.

Example 2 (*Comparison with the smoothing method*). Here we consider an example with zero jump conditions $[\phi] = 0$ and $[\sigma \phi_n] = 0$, and compare the numerical results with those from the smoothing method. By the smoothing method, we meant that Eq. (12) is solved by first smoothing σ through harmonic averaging as

$$\frac{1}{\sigma(\mathbf{x})} = \frac{H(\mathbf{x})}{\sigma^-} + \frac{1 - H(\mathbf{x})}{\sigma^+},$$

and then using the regular centered difference scheme to discretize the equation. Here, $H(\mathbf{x})$ is the indicator function (or regularized Heaviside function) which can be obtained by solving

$$\Delta H(\mathbf{x}) = -\nabla \cdot \int_{\Sigma} \mathbf{n} \delta(\mathbf{x} - \mathbf{X}(s)) |\mathbf{X}_s| \, ds.$$

In this case, the interface is chosen as a circle with radius 0.5 immersed in computational domain $[-1, 1] \times [-1, 1]$. The exact solution is given by

$$\phi(x, y) = \begin{cases} a_2(x^2 + y^2) + a_1 & \mathbf{x} \in \Omega^-, \\ (x^2 + y^2)^2 & \mathbf{x} \in \Omega^+. \end{cases}$$

The ratio is taken by $\sigma_r = 0.1$. The parameters a_1 and a_2 can be determined by setting the jump conditions $[\phi]$ and $[\sigma \phi_n]$ to be zero across the interface. From Table 2, one can see that the numerical solution from the smoothing method ϕ_h^S has first-order convergence while its derivatives do not seem to converge at all. This is not surprising since the derivative is discontinuous across the interface in the smoothing method. Both the solution (ϕ_h) and its derivative $(\phi_h)_x$ from our present IIM are more accurate than those from the smoothing method.

4. Numerical algorithm

To solve the whole electrohydrodynamic equations numerically, let us first perform the non-dimensionalization on those governing equations as in [11]. To proceed, we scale all physical variables by the associated characteristic scales as follows.

$$\mathbf{x}^* = \frac{\mathbf{x}}{R}, \qquad t^* = \sqrt{\frac{\gamma}{\rho R^3}} t, \qquad \mathbf{u}^* = \sqrt{\frac{\rho R}{\gamma}} \mathbf{u}, \qquad p^* = \frac{R}{\gamma} p, \qquad \varepsilon^* = \frac{\varepsilon}{\varepsilon^+}, \qquad \sigma^* = \frac{\sigma}{\sigma^+}, \qquad \mathbf{E}^* = \frac{\mathbf{E}}{|\mathbf{E}_\infty|}.$$

Here, R is the initial drop radius. After some simple calculations, the dimensionless governing equations become (after dropping $*$ in notations)

$$\frac{\partial \mathbf{u}}{\partial t} + (\mathbf{u} \cdot \nabla)\mathbf{u} + \nabla p = Oh \, \Delta \mathbf{u} + \int_{\Sigma} \big(\mathbf{F}_C + Ca_E \, \mathbf{F}_E |\mathbf{X}_s|\big) \delta\big(\mathbf{x} - \mathbf{X}(s,t)\big) \, ds \quad \text{in } \Omega, \tag{20}$$

$$\nabla \cdot \mathbf{u} = 0 \quad \text{in } \Omega, \tag{21}$$

$$\mathbf{F}_C = \frac{\partial}{\partial s}(\gamma \boldsymbol{\tau}) \quad \text{on } \Sigma, \tag{22}$$

$$\Delta \phi = 0 \quad \text{in } \Omega, \quad [\phi] = 0, \quad [\sigma \phi_n] = 0, \quad \text{on } \Sigma, \tag{23}$$

$$\mathbf{E} = -\nabla \phi, \qquad \mathbf{M}_E = \varepsilon\left(\mathbf{E}\mathbf{E} - \frac{1}{2}(\mathbf{E} \cdot \mathbf{E})I\right), \qquad \mathbf{F}_E = \big(\mathbf{M}_E^+ - \mathbf{M}_E^-\big) \cdot \mathbf{n}, \tag{24}$$

$$\frac{\partial \mathbf{X}}{\partial t}(s,t) = \mathbf{U}(s,t) = \int_{\Omega} \mathbf{u}(\mathbf{x},t)\delta\big(\mathbf{x} - \mathbf{X}(s,t)\big) \, d\mathbf{x} \quad \text{on } \Sigma. \tag{25}$$

There are two dimensionless numbers; namely, the Ohnesorge number, $Oh = \mu/\sqrt{\gamma \rho R}$ is the ratio of the viscous force to the inertia and surface tension force; and the electric capillary number, $Ca_E = \varepsilon^+ R|\mathbf{E}_\infty|^2/\gamma$ measures the strength of the electric field relative to the surface tension force.

Next, we describe a hybrid numerical scheme to solve the electrohydrodynamic equations Eqs. (20)–(25). The underlying idea is that the fluid equations are solved by usual immersed boundary method while the electric potential equation is solved by the proposed immersed interface method in Section 3. For simplicity, let us assume the computational domain to be a rectangular domain $\Omega = [a,b] \times [c,d]$. Within this domain, a uniform lattice grid with mesh width h is employed, and the fluid variables are defined in a staggered MAC manner [8]. That is, the velocity components u and v are defined at cell-normal edges $(x_{i-1/2}, y_j) = (a+(i-1)h, c+(j-1/2)h)$ and $(x_i, y_{j-1/2}) = (a+(i-1/2)h, c+(j-1)h)$, respectively, while the pressure p and the electric potential ϕ are both defined at the cell center $\mathbf{x} = (x_i, y_j) = (a+(i-1/2)h, c+(j-1/2)h)$.

Since the drop interface $\mathbf{X}(s) = (X(s), Y(s))$, $s \in [0, 2\pi]$ is closed (so periodic), we can use the spectral Fourier discretization to represent $X(s)$ and $Y(s)$. We first choose an even number of collocation points such that the interface is discretized by $\mathbf{X}(s_k) = (X(s_k), Y(s_k))$, where $s_k = k\Delta s$, $k = 0, 1, \ldots M$ with $\Delta s = 2\pi/M$. The interface can be represented in truncated Fourier series as

$$X(s) = \sum_{l=-M/2}^{M/2-1} \widehat{X}_l e^{ils}, \quad \text{and} \quad Y(s) = \sum_{l=-M/2}^{M/2-1} \widehat{Y}_l e^{ils}, \tag{26}$$

where $\widehat{X}_l$ and $\widehat{Y}_l$ are the corresponding Fourier coefficients for $X(s)$ and $Y(s)$, respectively, and can be computed very efficiently using the Fast Fourier Transform (FFT). Under the Fourier representation, the derivatives with respect to s can be computed quite easily by using the pseudospectral method [28]. The Fourier coefficients of p-th derivative of $X(s)$ are simply computed as $(il)^p \widehat{X}_l$. Similar procedures can be applied for the derivatives of $Y(s)$. In this fashion, all interfacial quantities such as the tangent vector $\boldsymbol{\tau}$ (thus, the normal vector $\mathbf{n}$) and the curvature κ can be computed with spectral accuracy. As demonstrated in our recent work [12] for a three-dimensional axisymmetric interface, the present spectral method for computing the curvature is indeed more accurate than the finite difference method (traditionally used in IB). In addition, this spectral representation of the interface is more advantageous when the surfactant is present along the interface since the surfactant convection-diffusion equation can be solved more accurately as well.

In the following, we describe how to advance one time step for the solution variables. At the beginning of each time step n, the interface position $\mathbf{X}^n$ and the fluid velocity $\mathbf{u}^n$ must be given. The numerical algorithm is as follows.

1. Compute the electric potential ϕ^n in Eq. (23) by the augmented IIM developed in Subsection 3.1. Use the values of ϕ^n to compute the electric field $\mathbf{E}^n = (-\phi_x^n, -\phi_y^n)$ on the grid. (At the irregular point, a correction term must be added to achieve the desired accuracy.) Then we perform one-sided interpolation to compute the Maxwell stresses $\mathbf{M}_E^+$ and $\mathbf{M}_E^-$ to obtain the interfacial electric force $\mathbf{F}_E^n$ at Lagrangian markers.
2. Given the interface markers $\mathbf{X}^n$, we first compute the unit tangent vector $\boldsymbol{\tau}^n$ and then compute the interfacial tension force $\mathbf{F}_C^n$ in Eq. (22). The above both terms involving spatial derivatives with respect to s can be computed with spectral accuracy.
3. Distribute the interfacial tension and electric force from the Lagrangian markers to the fluid grid points by using the discrete delta function as in traditional IB method.
4. Solve the Navier–Stokes equations by the pressure-increment projection method to obtain new velocity $\mathbf{u}^{n+1}$. This procedure involves solving two Helmholtz-type equations for the intermediate velocity and one Poisson equation for the pressure-increment which again can be efficiently done by applying the fast direct solver provided by Fishpack.
5. Interpolate the new velocity on the fluid grid points to the marker points and then move the markers to new positions $\mathbf{X}^{n+1}$ as in Eq. (25).

Here, the detailed numerical implementation of Step 1 is described in Subsection 3.1 while Steps 2–5 are quite standard in immersed boundary method and can be found in any related literature such as in [16,12].
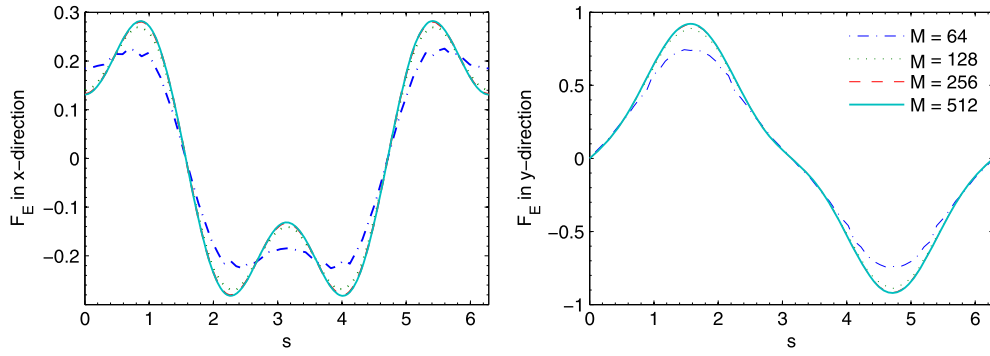
Fig. 3. Electric force $\mathbf{F}_E$ at different number of markers $M = 64, 128, 256$ and 512. Left panel is the x component and right panel is the y component. $M = 64$ for dash-dotted lines, $M = 128$ for dotted lines, $M = 256$ for dashed lines, and $M = 512$ for solid lines.

Remark. In the context of immersed boundary simulations, the interface is usually evolved by tracking the interface markers in a Lagrangian manner. Once the initial positions of the Lagrangian markers are chosen, the movement of those markers is determined by the interpolated local fluid velocity. Very often, as time evolves, these Lagrangian markers may be either clustered or dispersed in some regions. For example, our numerical results in the next section show that a homogeneous DC electric field induces a circulatory flow inside the viscous leaky dielectric drop, moving from the equator toward the tips and the Lagrangian markers are densely clustered around the tip regions. As a result, the overall numerical stability and accuracy may suffer at later times. To avoid such clustering of Lagrangian markers, we have introduced an artificial tangential velocity $U^A(s, t)$ into Eq. (25) as

$$\frac{\partial \mathbf{X}(s, t)}{\partial t} = \mathbf{U}(s, t) + U^A(s, t)\boldsymbol{\tau}, \tag{27}$$

so that the Lagrangian markers can be uniformly distributed. Here, the term $U^A(s, t)$ has the form of

$$U^A(s, t) = \frac{s}{2\pi} \int_0^{2\pi} \frac{\partial \mathbf{U}}{\partial s'} \cdot \boldsymbol{\tau}' \, \mathrm{d}s' - \int_0^s \frac{\partial \mathbf{U}}{\partial s'} \cdot \boldsymbol{\tau}' \, \mathrm{d}s'. \tag{28}$$

The detailed derivation for the above tangential velocity can be found in [16].

5. Numerical results

In this section, we perform a series of numerical tests for the present scheme developed in the previous section. We first verify the convergence of the interfacial electric force and the fluid variables. Then, we run a series of simulations with different permittivity ratio $\varepsilon_r = \varepsilon^-/\varepsilon^+$ and conductivity ratio $\sigma_r = \sigma^-/\sigma^+$, and compare the results with the ones obtained by the small deformation theory. We also study the electric effect for a drop under shear flow. Finally, we study some drop deformations by slightly increasing the electric capillary number Ca_E to see how the drop behaves and compare with other numerical results in literature. Throughout this paper, we put a circular drop with the radius $R = 1$ inside the fluid domain $\Omega = [-4, 4] \times [-4, 4]$ and set the initial velocity to be zero everywhere. The flow is simply driven by the electrical field. The boundary condition for the velocity field is zero (except the one for the shear flow which is indicated in Fig. 7). The far electric field is chosen as $\mathbf{E}_\infty = (0, -1)$ so the boundary conditions for the potential ϕ are $\phi = y$ (Dirichlet) at $y = \pm 4$, and $\frac{\partial \phi}{\partial x} = 0$ (Neumann) at $x = \pm 4$. The Cartesian grid mesh width h for the fluid variables and the potential is now defined as $h = 8/N$ in both x and y directions with the grid size N. There are M Lagrangian markers distributed initially along the interface with the Lagrangian mesh $\Delta s = 2\pi/M < h$. Here, we simply choose $M = N$ in all simulations. The time step is chosen as $\Delta t = h/4$. The Ohnesorge number is chosen as $Oh = 1$, the surface tension $\gamma = 1$ and the electric capillary number $Ca_E = 0.5$ unless otherwise stated.

5.1. Convergence test for the interfacial electric force $\mathbf{F}_E$

As mentioned in Section 2.1, the electric field effects are incorporated as an electric interfacial force $\mathbf{F}_E$ in Eq. (10) instead of the more conventional approach in [11,31]. In this simulation, we set $\sigma_r = 3$ and $\varepsilon_r = 2$, and plot $\mathbf{F}_E$ in Fig. 3 with different number of Lagrangian markers $M = 64, 128, 256$ and 512. One can see that the interfacial electric force tends to converge as the marker size M increases. In addition, we plot the successive errors defined by $\|(\mathbf{F}_E)_{2M} - (\mathbf{F}_E)_M\|_\infty$ versus the marker size M in Fig. 4. Again, roughly second-order convergence has been observed in this test.
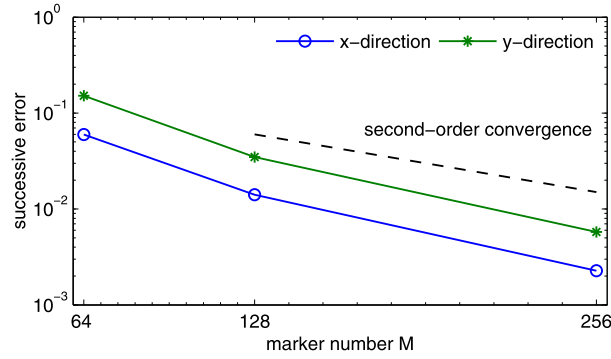
Fig. 4. The successive errors of the electric interfacial force $\mathbf{F}_E$ in both x and y directions (see legends). The rate of convergence is around second-order.

Table 3
The mesh refinement results for the velocity components u and v, the interface configuration $\mathbf{X}$, and the relative volume loss of the drop at $T = 2$.

N	$\|u_{2N} - u_N\|_\infty$	Rate	$\|v_{2N} - v_N\|_\infty$	Rate	$\|\mathbf{X}_{2N} - \mathbf{X}_N\|_\infty$	Rate	$\frac{|A_N - A_0|}{A_0}$
64	1.19E−02	–	1.62E−02	–	3.01E−02	–	8.74E−05
128	2.84E−03	2.07	5.36E−03	1.60	8.80E−03	1.78	5.85E−05
256	7.77E−04	1.87	8.85E−04	2.60	1.41E−03	2.64	3.16E−05

5.2. Convergence test for the fluid variables

In this subsection, we perform the convergence test for the present numerical algorithm of the whole electrohydrodynamic equations. We again choose the conductivity ratio $\sigma_r = 3$ and permittivity ratio $\varepsilon_r = 2$ with different number of grid points $N = 64, 128, 256, 512$. All the numerical solutions are computed up to time $T = 2$. Since the analytical solutions are not available in this test, we compute the errors between two successive grids denoted by $\|u_{2N} - u_N\|$ so the rate of convergence is calculated by rate $= \log_2 \frac{\|u_N - u_{N/2}\|}{\|u_{2N} - u_N\|}$. The errors and ratios of v and the interface configuration $\mathbf{X}$ are all computed in the same manner. Table 3 shows the maximum errors for the fluid velocity and the interface configuration. Note that, the fluid variables are defined on the staggered grid. Thus, when we refine the mesh, the numerical solutions will not coincide with the same grid locations and a simple bi-linear interpolation must be implemented. Due to the fact that the immersed boundary formulation has the singular forcing term in the equations, regularizing the singular term by smoothing discrete delta functions might cause the method to be first-order accurate. However, the present numerical results show better than first-order convergence.

Meanwhile, we also check the volume (area in 2D) loss of the drop in our present computations. From Table 3 (last column), one sees that the relative volume loss is of order of magnitude 10^{-5} which is negligibly small in present simulations. We attribute such good volume-conservation behavior to the choice of fluid solver and the enforcement of uniformly distributed Lagrangian markers. Very recently, Boyce Griffith [7] has performed rather detailed numerical tests on volume-conservation for different IB implementations. In our work the pressure-increment projection method under staggered grid discretization is adopted for our fluid solver because of its superior performance for volume-conservation [7].

5.3. Comparison with small-deformation theory

In this subsection, we simulate the drop deformation under a DC electric field, and compare with asymptotic results from the small-deformation theory. G.I. Taylor [27] developed a linear model to compute steady equilibrium shape of a leaky dielectric drop under a DC electric field. He found that the viscous drop can turn into either oblate or prolate shape. Based on Taylor's asymptotic results, the drop deformation depends on the electric capillary number Ca_E, the ratio of electric conductivity, permittivity, and fluid viscosity. The equilibrium drop deformation can be quantified by the drop deformation number D as

$$D = \frac{L - B}{L + B},$$

where L and B are the drop deformations along the major and minor axes, respectively. The first-order small-deformation model for a two-dimensional viscous drop is developed by Feng [6] (also listed in [36]) and is analogous to Taylor's linear model for a spherical drop [27]. In this linear model the equilibrium drop deformation is approximated by

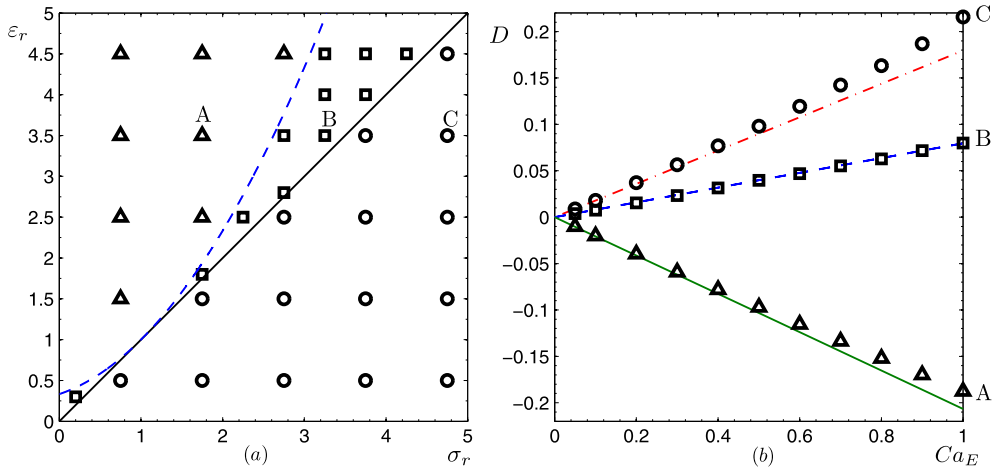$$D = \frac{f_d(\sigma_r, \varepsilon_r)}{3(1 + \sigma_r)^2} Ca_E, \tag{29}$$

Fig. 5. (a) The drop shape diagram for different conductivity ratio σ_r and permittivity ratio ε_r. Solid line: $\sigma_r = \varepsilon_r$; dashed line: $f_d = 0$. "△": Oblate and clockwise; "□": prolate and clockwise (prolate B); "○": prolate and counterclockwise (prolate A). (b) The plot of the deformation number D versus the electric capillary number Ca_E. These lines are the theoretical results from the two-dimensional small-deformation theory [6].

where f_d is a discriminating function defined by $f_d(\sigma_r, \varepsilon_r) = \sigma_r^2 + \sigma_r + 1 - 3\varepsilon_r$. The discriminating function f_d indicates the equilibrium drop shape; that is, $f_d > 0$, the prolate shape is obtained while $f_d < 0$ the oblate shape is obtained. $f_d = 0$ indicates the drop remains spherical at leading order. Under a DC electric field, a circulatory flow motion is needed to balance the electric stress when the drop reaches a steady equilibrium. For the oblate drop, the circulatory flow pattern inside the first quadrant is always clockwise, while the flow for the prolate one is either clockwise ($\sigma_r < \varepsilon_r$) or counterclockwise ($\sigma_r > \varepsilon_r$).

For the following simulation results, the number of grid point is fixed as $N = 128$ and the simulations are started from the same initial condition (circular shape) until a steady equilibrium state is achieved. Fig. 5(a) shows the equilibrium drop shape diagram and circulatory flow patterns (as labeled) for the drop under DC electric field on the σ_r–ε_r plane. Our numerical simulation results confirm the predictions from the small-deformation theory. Such agreement validates our hybrid numerical schemes.

In Fig. 5(a) three cases in different parameter regimes are labeled: Case A ($\sigma_r = 1.75$, $\varepsilon_r = 3.5$), Case B ($\sigma_r = 3.25$, $\varepsilon_r = 3.5$), and Case C ($\sigma_r = 4.75$, $\varepsilon_r = 3.5$). For these three cases, we conduct the simulations with different electric capillary number Ca_E. Fig. 5(b) shows the deformation number D versus the electric capillary number Ca_E for these three cases. Notice that, the deformation number D is negative when the shape is oblate while D is positive when the shape is prolate. As expected, the steady deformation becomes larger as the electric capillary number Ca_E increases. We also plot the theoretical results based on small deformation theory (Eq. (29)) for these three cases. One can see that the present numerical results agree well with the theoretical ones when Ca_E is small. This is not surprising since the theoretical result is applicable only for small drop deformation.

Fig. 6 shows the drop shapes and flow patterns at different times for the above Cases A, B, and C. In each subplot, the velocity quivers are depicted in the right half while the corresponding stream lines are shown in the left. One can immediately see that when the drop shape is oblate (Case A), the induced circulatory flow inside the first quadrant is clockwise (from the pole to the equator). However, for the prolate shape, the induced circulatory flow can be clockwise (Case B) and counterclockwise (from the equator to the pole, Case C). Again, these flow patterns are in good agreement with those from the theoretical models.

5.4. A leaky dielectric drop under a DC field and a shear flow

If a shear flow and electric field are simultaneously applied to the drop, the drop deformation and orientation will be affected by the relative strength of the shear and electric stresses. As we see from results in Section 5.3, the applied electric field aligns the drop and elongates its shape either parallel (prolate) or perpendicular (oblate) to the electric field. When a shear flow is applied, one can imagine that the drop rotates to orient along the extensional direction in the shear flow. Fig. 7 shows the comparison for the drop shapes under shear flow with (denoted by solid line) or without (dashed line) the electric field. Here, all the parameters used are exactly same as the ones in Fig. 6. Under the electric field, we observe that for the oblate Case A (top row), the drop tends to tilt horizontally along the shear flow direction, while for prolate Case B (middle row) and Case C (bottom row), the drops tend to tilt vertically instead.
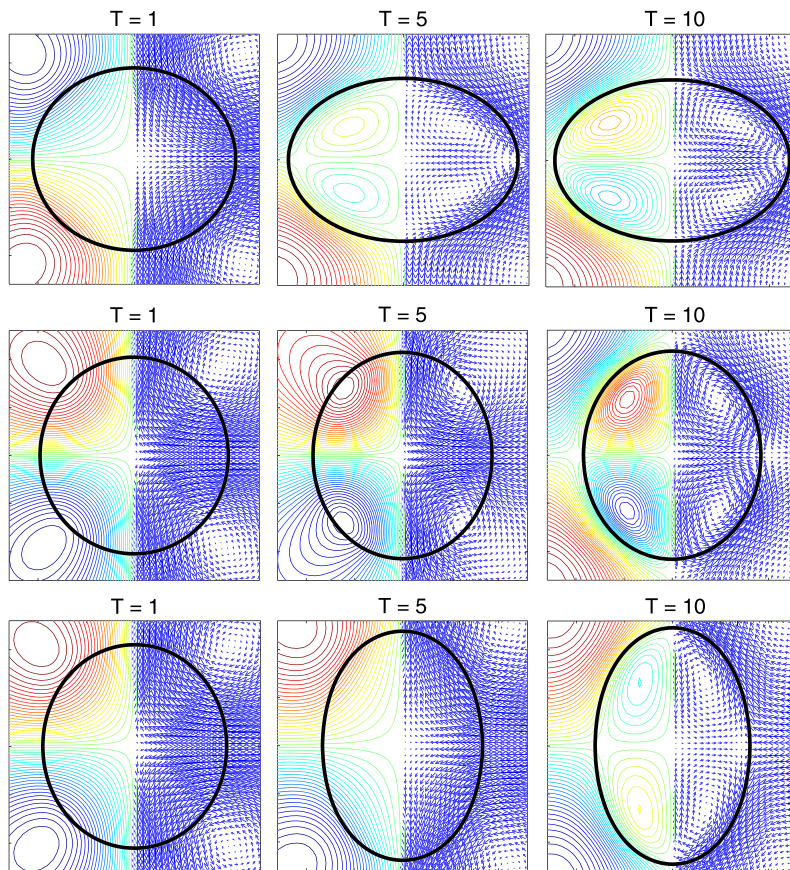
Fig. 6. Drop shapes and flow patterns for Cases A, B, and C at different times. Top row: Case A ($\sigma_r = 1.75$, $\varepsilon_r = 3.5$), oblate and clockwise; Middle row: Case B ($\sigma_r = 3.25$, $\varepsilon_r = 3.5$), prolate and clockwise; Bottom row: Case C ($\sigma_r = 4.75$, $\varepsilon_r = 3.5$), prolate and counterclockwise. $Ca_E = 1$.

5.5. Large deformation of drop dynamics

In this subsection, we investigate the large deformation of a viscous drop under a strong electric field (high Ca_E). Lac and Homsy used the boundary integral method to study the axisymmetric deformation of a drop under a DC electric field. Their boundary integral simulations showed that the drop stays spheroidal and its deformation increases with Ca_E until a critical value, beyond which the drop either takes a non-spheroidal axisymmetric equilibrium shape or breaks up into smaller droplets [13]. On the other hand, they also found that under certain (σ_r, ε_r) regimes, the drop break-up process may not occur as Ca_E increases. Here, we choose the non-breakup parameters for both prolate ($\sigma_r = 10$, $\varepsilon_r = 1.37$) and oblate ($\sigma_r = 0.6$, $\varepsilon_r = 1.37$) drops, and study their large deformations. The electric capillary number $Ca_E = 2$ is chosen slightly higher than previous tests. One can see from Fig. 8 that both drops deform into an elongated peanut-like shape at equilibrium. The numerical results are qualitatively consistent with those in [13], even though our simulations are two-dimensional while their boundary integral simulation results are axisymmetric [13].

6. Conclusions

In this paper, we have developed a hybrid immersed boundary (IB) and immersed interface method (IIM) to simulate the dynamics of a leaky dielectric drop in Navier–Stokes flows. The electric potential is solved numerically by an augmented IIM which incorporates the jump conditions naturally along the normal direction. Instead of applying the volume electric force arising from the Maxwell stress tensor, we alternatively treat the electric effect as an interfacial force bearing the normal jump of Maxwell stress on the interface. Thus, we can put the capillary and electric forces in a unified immersed boundary formulation, which greatly simplifies the numerical algorithm for the full system. We first computed the potential and its gradient (electric field) to perform the accuracy check for the present IIM. We further checked the convergence of the interfacial electric force and the fluid variables. We ran a series of simulations with different permittivity and conductivity ratios and compared the results obtained by the small deformation theory and other numerical results in literature. Our results show good agreement with theoretical models and other numerical results. In addition, we also studied the electric effect on a drop under shear flow.
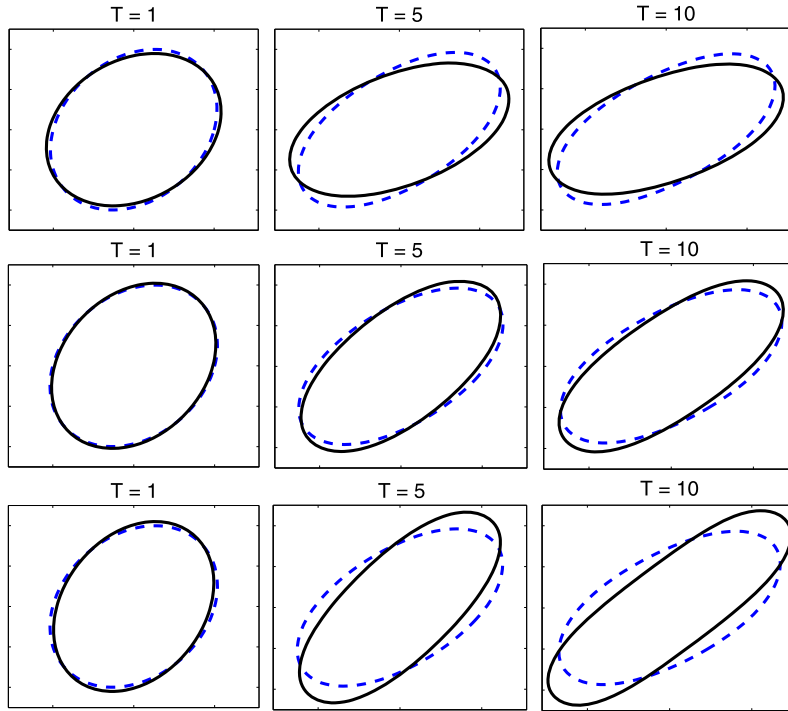
Fig. 7. The snapshots for a drop under both an electric field (vertical) and shear flow (horizontal) $\mathbf{u} = (0.3y, 0)$ with (solid line) or without (dashed line) the electric effect. Top row: Case A; Middle row: Case B; Bottom row: Case C. $Ca_E = 1$.
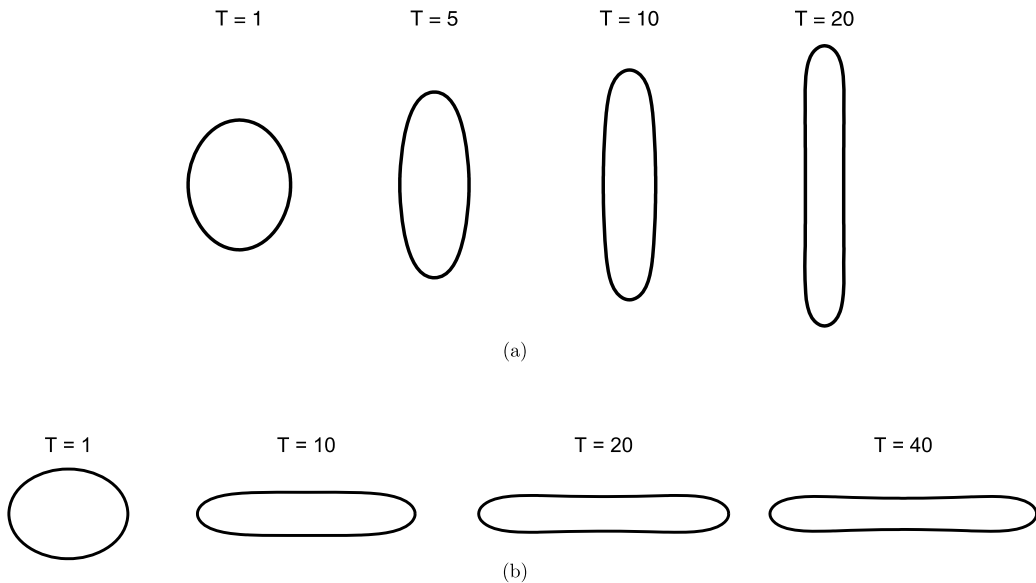

Fig. 8. Drop deformation with $Ca_E = 2$ at different times: (a) $\sigma_r = 10$, $\varepsilon_r = 1.37$, and (b) $\sigma_r = 0.6$, $\varepsilon_r = 1.37$.

In this paper, we mainly consider a neutrally buoyant drop suspended in a fluid with matching density and viscosity but with different permittivity and conductivity subject to a DC electric field. Certainly, we can consider the cases with mismatched density and viscosity for the drop and suspended fluid by adopting different fluid solvers. It has been observed in experiments [26] that with different viscosity for the drop and suspended fluid, the drop will be tilted with respect to the electric field direction as long as the electric field is strong enough. As a result, the drop shape becomes non-axisymmetric and a rotational flow is induced about the drop. To model this problem, one needs to take the surface charge convection effect into account in our present formulation. However, as far as the scheme developed in this work is concerned, the major ingredients and contributions will remain identical. We leave this extension as our future work.

Acknowledgements

Appendix A

In the appendix, we express the interfacial electric force explicitly and show that the mathematical form is exactly the same used in [32]. Let us write the electric flux density $\mathbf{J} = \sigma \mathbf{E}$ and express $\mathbf{E} = E_n \mathbf{n} + E_\tau \boldsymbol{\tau}$ where E_n and E_τ are the normal and tangent components of the electrical field. Substituting the above expression of $\mathbf{E}$ into the definition of Maxwell stress tensor of Eq. (8) and multiplying the normal vector $\mathbf{n}$, we can obtain

$$
\begin{aligned}
\mathbf{M}_E \cdot \mathbf{n} &= \varepsilon \left(\mathbf{EE} - \frac{1}{2} (\mathbf{E} \cdot \mathbf{E}) I \right) \cdot \mathbf{n} \\
&= \varepsilon E_n (E_n \mathbf{n} + E_\tau \boldsymbol{\tau}) - \frac{\varepsilon}{2} \left(E_n^2 + E_\tau^2 \right) \mathbf{n} \\
&= \frac{\varepsilon}{\sigma^2} (\sigma E_n)^2 \mathbf{n} + \frac{\varepsilon}{\sigma} (\sigma E_n) E_\tau \boldsymbol{\tau} - \frac{\varepsilon}{2\sigma^2} (\sigma E_n)^2 \mathbf{n} - \frac{\varepsilon}{2} E_\tau^2 \mathbf{n} \\
&= \frac{\varepsilon}{2\sigma^2} (\sigma E_n)^2 \mathbf{n} + \frac{\varepsilon}{\sigma} (\sigma E_n) E_\tau \boldsymbol{\tau} - \frac{\varepsilon}{2} E_\tau^2 \mathbf{n} \\
&= \frac{1}{2} \left(J_n^2 \frac{\varepsilon}{\sigma^2} - E_\tau^2 \varepsilon \right) \mathbf{n} + \frac{\varepsilon}{\sigma} J_n E_\tau \boldsymbol{\tau} \quad \text{where } J_n = \mathbf{J} \cdot \mathbf{n}.
\end{aligned}
$$

The zero jump conditions of Eq. (7) imply that the tangential component of the electric field E_τ and the electric flux density J_n are both continuous across the interface; that is $[E_\tau] = 0$ and $[J_n] = 0$. Thus, the interfacial electric force can be written as

$$
\begin{aligned}
\mathbf{F}_E &= \left(\mathbf{M}_E^+ - \mathbf{M}_E^- \right) \cdot \mathbf{n} \\
&= \frac{1}{2} \left(J_n^2 \left(\frac{\varepsilon^+}{(\sigma^+)^2} - \frac{\varepsilon^-}{(\sigma^-)^2} \right) - E_\tau^2 (\varepsilon^+ - \varepsilon^-) \right) \mathbf{n} + J_n E_\tau \left(\frac{\varepsilon^+}{\sigma^+} - \frac{\varepsilon^-}{\sigma^-} \right) \boldsymbol{\tau}.
\end{aligned}
$$

This is exactly the same form as the continuous electric surface force shown in Eq. (19) of Tomar et al. [32].

References

[1] J. Adams, P. Swarztrauber, R. Sweet, Fishpack – a package of Fortran subprograms for the solution of separable elliptic partial differential equations, available at http://www.netlib.org/fishpack, 1980.
[2] J.T. Beale, A.T. Layton, On the accuracy of finite difference methods for elliptic problems with interfaces, Commun. Appl. Math. Comput. Sci. 1 (2006) 91–119.
[3] A.P.S. Bhalla, R. Bale, B.E. Griffith, N.A. Patankar, Fully resolved immersed electrohydrodynamics for particle motion, electrolocation, and self-propulsion, J. Comput. Phys. 256 (2014) 88–108.
[4] E. Bjorklund, The level set method applied to droplet dynamics in the presence of an electric field, Comput. Fluids 38 (2009) 358–369.
[5] K.-Y. Chen, M.-C. Lai, A conservative scheme for solving coupled surface-bulk convection–diffusion equations with an application to interfacial flows with soluble surfactant, J. Comput. Phys. 257 (2014) 1–18.
[6] J.Q. Feng, A 2D electrohydrodynamic model for electrorotation of fluid drops, J. Colloid Interface Sci. 246 (2002) 112–121.
[7] B.E. Griffith, On the volume conservation of the immersed boundary method, Commun. Comput. Phys. 12 (2012) 401–432.
[8] F.H. Harlow, J.E. Welsh, Numerical calculation of time-dependent viscous incompressible flow of fluid with a free surface, Phys. Fluids 8 (1965) 2181–2189.
[9] J.M. Lopez-Herrera, S. Popinet, M.A. Herrada, A charge-conservative approach for simulating electrohydrodynamic two-phase flows using volume-of-fluid, J. Comput. Phys. 230 (2011) 1939–1955.
[10] M.R. Hossan, R. Dillon, A.K. Roy, P. Dutta, Modeling and simulation of dielectrophoretic particle–particle interactions and assembly, J. Colloid Interface Sci. 394 (2013) 619–629.
[11] J. Hua, L.K. Lim, C.-H. Wang, Numerical simulation of deformation/motion of a drop suspended in viscous liquids under influence of steady electric fields, Phys. Fluids 20 (2008) 113302.
[12] W.-F. Hu, Y. Kim, M.-C. Lai, An immersed boundary method for simulating the dynamics of three-dimensional axisymmetric vesicles in Navier–Stokes flows, J. Comput. Phys. 257 (2014) 670–686.
[13] E. Lac, G.M. Homsy, Axisymmetric deformation and stability of a viscous drop in a steady electric field, J. Fluid Mech. 590 (2007) 239–264.
[14] M.-C. Lai, H.-C. Tseng, A simple implementation of the immersed interface methods for Stokes flows with singular forces, Comput. Fluids 37 (2008) 99–106.
[15] M.-C. Lai, Y.-H. Tseng, H. Huang, An immersed boundary method for interfacial flows with insoluble surfactant, J. Comput. Phys. 227 (2008) 7279–7293.
[16] M.-C. Lai, Y.-H. Tseng, H. Huang, Numerical simulation of moving contact lines with surfactant by immersed boundary method, Commun. Comput. Phys. 8 (2010) 735–757.
[17] Z. Li, K. Ito, The Immersed Interface Method, SIAM, 2006.
[18] Y. Lin, P. Skjetne, A. Carlson, A phase field model for multiphase electro-hydrodynamics flow, J. Multiph. Flow 45 (2012) 1–11.
[19] L.C. McConnell, M. Miksis, Vesicle electrohydrodynamics in DC electric fields, IMA J. Appl. Math. (2013) 1–21.
[20] J.R. Melcher, G.I. Taylor, Electrohydrodynamics: a review of the role of interfacial shear stresses, Annu. Rev. Fluid Mech. 1 (1969) 111.

[21] H. Nganguia, Y.-N. Young, P.M. Vlahovska, J. Bławzdziewcz, J. Zhang, H. Lin, Equilibrium electro-deformation of a surfactant-laden viscous drop, Phys. Fluids 25 (2013) 092105.
[22] A. Ramos (Ed.), Electrokinetics and Electrohydrodynamics in Microsystems, Springer, 2011.
[23] D. Russel, Z.J. Wang, A Cartesian grid method for modeling multiple moving objects in 2D incompressible viscous flow, J. Comput. Phys. 191 (2003) 177–205.
[24] D.A. Saville, Electrohydrodynamics: the Taylor–Melcher leaky dielectric model, Annu. Rev. Fluid Mech. 29 (1997) 27.
[25] J. Sherwood, Breakup of fluid droplets in electric and magnetic fields, J. Fluid Mech. 188 (1988) 133–146.
[26] P.F. Salipante, P.M. Vlahovska, Electrohydrodynamics of drops in strong uniform dc electric fields, Phys. Fluids 22 (2010) 112110.
[27] G.I. Taylor, Studies in electrohydrodynamics I. The circulation produced in a drop by an electric field, Proc. R. Soc. Lond. A 291 (1966) 159.
[28] L.N. Trefethen, Spectral Methods in MATLAB, SIAM, Philadelphia, 2000.
[29] S. Torza, R.G. Fox, S.G. Mason, Electrohydrodynamic deformation and burst of liquid drops, Philos. Trans. R. Soc. Lond. A 269 (1971) 295–319.
[30] G. Tryggvason, A. Fernandez, J. Lu, The effect of electrostatic forces on droplet suspensions, Comput. Fluid Solid Mech. (2003) 1166–1168.
[31] K.E. Teigen, S.T. Munkejord, Influence of surfactant on drop deformation in an electric field, Phys. Fluids 22 (2010) 112104.
[32] G. Tomar, D. Gerlach, G. Biswas, N. Alleborn, A. Sharma, F. Durst, S.W.J. Welch, A. Delgado, Two-phase electrohydrodynamic simulations using a volume-of-fluid approach, J. Comput. Phys. 227 (2007) 1267–1285.
[33] H.H. Woodson, J.R. Melcher, Electromechanical Dynamics, John Wiley and Sons, 1968.
[34] S. Xu, An iterative two-fluid pressure solver based on the immersed interface method, Commun. Comput. Phys. 12 (2012) 528–543.
[35] Q. Yang, B.Q. Li, Y. Ding, 3D phase field modeling of electrohydrodynamic multiphase flows, Int. J. Multiph. Flow 57 (2013) 1–9.
[36] J. Zhang, D.Y. Kwok, A 2D lattice Boltzmann study on electrohydrodynamic drop deformation with the leaky dielectric theory, J. Comput. Phys. 206 (2005) 150–161.